

Chaotic Vibration of a Quarter-Car Model Excited by the Road Surface Profile

Grzegorz Litak,^{a,1} Marek Borowiec,^a Michael I. Friswell^b
Kazimierz Szabelski^a

^a*Department of Applied Mechanics, Technical University of Lublin, Nadbystrzycka
36, PL-20-618 Lublin, Poland*

^b*Department of Aerospace Engineering, University of Bristol, Queens Building,
Bristol BS8 1TR, United Kingdom*

Abstract

The Melnikov criterion is used to examine a global homoclinic bifurcation and transition to chaos in the case of a quarter car model excited kinematically by the road surface profile. By analyzing the potential an analytic expression is found for the homoclinic orbit. By introducing an harmonic excitation term and damping as perturbations, the critical Melnikov amplitude of the road surface profile is found, above which the system can vibrate chaotically.

Keywords: Melnikov criterion, chaotic vibration, quarter-car, sky hook, magnetorheological dampers

1 Introduction

The problem of rough surface road profiles and its influence on vehicle unwanted vibrations due to kinematic excitations is still a subject of research among automotive manufacturers and research groups, whose objective is to minimize their effects on the driver and passengers [1–6]. Past studies focused on the dynamics of a passive car suspension, the nonlinear characteristics of tyres and the effect of shimming in vehicle wheels [7–9]. Recently many new applications of active and semi active control procedures and special devices to minimize vehicle vibrations have been developed [10–12]. Consequently old mechanical quarter car models [8,9] have been re-examined in the context of active damper applications. Dampers based on magnetorheological fluid with

¹ Fax: +48-815250808; E-mail: g.litak@pollub.pl (G. Litak)

typical hysteretic characteristics have significant promise for effective vibration damping in many applications [13–15]. New ideas in vehicle vibration damping, such as 'Sky hook' control [16] or H_∞ control [15,17] have already been implemented and tested in several car and motorcycle applications. Efforts have focused on studies of the excitation of the automobile by a road surface profile with harmful noise components [3,4]. However, due to various nonlinearities in the vehicle dynamics, chaotic behaviour may produce noise like responses [6,18,19].

In the present paper the model of Li *et al.* [6] is used, with the addition of a gravitational term that changes the equilibrium point and therefore the external potential. This paper uses the Melnikov theory [20–22] to estimate the critical amplitude of the road surface profile above which the system can vibrate chaotically.

The gravitational term changes the topology of the heteroclinic orbit (in the case of a symmetric reversed 'Mexican hat' potential) into a homoclinic one (with a broken symmetry potential). Systems with Duffing characteristics having non-symmetric potentials and a linear repulsive force term are a wide class of mechanical systems and have been the subject of previous investigations in the context of the appearance of chaotic solutions [23–25,28]. This paper uses a similar approach for a quarter car model with a magnetorheological damper [13–15].

2 The quarter-car model

The equation of motion of a single degree of freedom quarter-car model (Fig. 1) is [6]

$$m \frac{d^2x}{dt^2} + k_1(x - x_0) + mg + F_h \left(\frac{d}{dt}(x - x_0), x - x_0 \right) = 0, \quad (1)$$

where F_h is an additional nonlinear hysteretic suspension damping and stiffness force dependent on relative displacement and velocity, given by

$$F_h \left(\frac{d}{dt}(x - x_0), x - x_0 \right) = k_2(x - x_0)^3 + c_1 \frac{d}{dt}(x - x_0) + c_2 \left(\frac{d}{dt}(x - x_0) \right)^3 \quad (2)$$

and

$$x_0 = A \sin(\Omega t). \quad (3)$$

Defining a new variable for a relative displacement as

$$y = x - x_0 \quad (4)$$

we get

$$\frac{d^2y}{dt^2} + \omega^2 y + B_1 y^3 + B_2 \frac{dy}{dt} + B_3 \left(\frac{dy}{dt} \right)^3 = -g + A\Omega^2 \sin(\Omega t), \quad (5)$$

where $\omega^2 = k_1/m$, $B_1 = k_2/m$, $B_2 = c_1/m$, $B_3 = c_2/m$.

Following Li *et al.* [6] the system parameters are defined as

$$\begin{aligned} m &= 240 \text{ kg}, \quad k_1 = 160000 \text{ N/m}, \quad k_2 = -300000 \text{ N/m}^3, \\ c_1 &= -250 \text{ Ns/m}, \quad c_2 = 25 \text{ Ns}^3/\text{m}^3. \end{aligned} \quad (6)$$

The corresponding dimensionless equation of motion can be written for a scaled time variable $\tau = \omega t$ as:

$$\ddot{y} + y + ky^3 + \alpha\dot{y} + \beta\dot{y}^3 = -g' + A\Omega'^2 \sin(\Omega'\tau), \quad (7)$$

where $k = B_1/\omega^2 = \frac{k_2}{k_1}$, $\alpha = B_2/\omega = \frac{c_1}{\sqrt{k_1 m}}$, $\beta = B_3 \omega = c_2 \sqrt{\frac{k_1}{m^3}}$, $g' = \frac{g}{\omega^2}$, $\Omega' = \Omega/\omega$. The overdots in Eq. (7) denote the corresponding derivative with respect to τ ($\dot{\cdot} \equiv d/d\tau$).

Note that in our model, Eq. (5), we use both a complicated non-symmetric potential and also non-trivial damping of the Rayleigh type. Similar damping terms have been used before in the context of Melnikov theory [29,30]. Litak *et al.* [29] considered the Froude pendulum, with polynomial damping to model a dry friction phenomenon. Trueba *et al.* [30] performed systematic studies for basic nonlinear oscillators including those with combined damping. Here the motivation in using a complicated damping term is different, and arises from the use of magnetorheological dampers in vehicle suspensions [13–15]. The signs of the c_i coefficients (Eqs. 1-2) have changed compared to reference [6], in order to recover the usual Rayleigh term $c_2 v^3 + c_1 v$, where $v = dy/dt$ is the system velocity and $c_1 < 0$, $c_2 > 0$ (defined Eq. (6)). This term is able to drive the system into a stable limit cycle solution, being dissipative for a large enough velocity v ($v > \sqrt{c_1/c_2}$) and pumping energy for a small velocity ($v < \sqrt{c_1/c_2}$).

In Eq. (7), the nonlinear stiffness force has the potential

$$V(y) = g'y + \frac{1}{2}y^2 + \frac{k}{4}y^4. \quad (8)$$

Figure 2 shows this potential, and highlights the characteristic fixed points. Note the non-symmetry is caused by the gravitational term $g'y$, and that $k < 0$.

In Figs. 3a-b we show the results of calculations in the interesting region of the main resonance for the system parameters given in Eq. (6) and a realistic amplitude of road profile excitation, namely $A = 0.11$ m. In this case the vehicle vibration amplitude, A_{OUT} , plotted in Fig. 3a, has been determined numerically. For simplicity it has been defined as:

$$A_{OUT} = (y_{max} - y_{min})/2, \quad (9)$$

where y_{max} and y_{min} are the maximum and minimum response of the vehicle model in the steady state. The resonance curve was calculated by tracking the solution for decreasing Ω' , and indicates that the main resonance occurs at $\Omega' \approx 0.85$. The response curve is inclined to the left, as expected for a nonlinear system with softening stiffness characteristic. Clearly, a jump between large and small vibration amplitudes exists at $\Omega' \approx 0.8$. Below this frequency we also observe a second, but much smaller, maximum of A_{OUT} (at $\Omega' \approx 0.75$) which indicates that something interesting is occurring at this frequency. To examine this effect in more detail Fig. 3b shows a bifurcation diagram over the same range of excitation frequencies. Interestingly $\Omega' \approx 0.75$ is a point of dramatic change in the system behaviour. For any frequency below this point we see a black bounded region while above it there are singular points. One can easily see that the local change in A_{OUT} is associated with a Hopf bifurcation. This transition is usually connected with a synchronization phenomenon between the system vibration frequency and the external excitation frequency. It is also connected with a slight change of the size of the attractor, reflected in the plot of $A_{OUT}(\Omega')$ (Fig. 3a).

To show the changes in the dynamics caused by this resonance and Hopf bifurcation, Figs. 4a-c show the phase portraits and Poincare maps of the system for three chosen frequencies. One can easily identify Fig. 4a ($\Omega' = 0.6$) as a quasi-periodic solution with a limit cycle attractor. On the other hand the solutions presented in Fig. 4b ($\Omega' = 0.8$) and Fig. 4c ($\Omega' = 1.1$) show synchronized motion represented by singular points. The range of the vibration amplitudes is the highest for the last case examined ($\Omega' = 1.1$), which is consistent with Fig. 3a.

Figure 4d shows the hysteresis of the function $F_h(\dot{y}, y)$, defined by Eq. (2) and obtained during the same simulation sweeps as the phase portraits. The corresponding hysteresis loops differ in size. Starting with '1' plotted for $\Omega' = 0.6$ then increasing strongly in size ('2' plotted for $\Omega' = 0.8$) and finally decreasing ('3' plotted for $\Omega' = 1.1$). Note this sequence differs from the changes in the vibration amplitude, where $\Omega' = 1.1$ has the largest amplitude, A_{OUT} , and this arises because of the combined effect of displacement and velocity.

3 Melnikov Analysis

Melnikov analysis starts with the renormalisation of the potential (Eq. (8), Fig. 2) [28]. If we let $y = z + y_0$, where y_0 is the fixed point given in Fig. 2, and $V_1(z) = V(y) - V(y_0)$, then,

$$V_1(z) = \frac{k}{4}z^2(z - z_1)(z - z_2), \quad (10)$$

where $z_1 = 1.298$ and $z_2 = 1.593$. Fig. 5 shows this normalized potential. Notice that the left peak (the saddle point) of the potential $V_1(z)$ occurs at $z = 0 < z_1 < z_2$ and that $V_1(0) = 0$.

Looking for a homoclinic orbit we introduce a small parameter ϵ (formally $\epsilon\tilde{\alpha} = \alpha$, $\epsilon\tilde{\beta} = \beta$ and $\epsilon\tilde{A} = A$). The equation of motion then has the following form,

$$\ddot{z} + \epsilon\tilde{\alpha}\dot{z} + \epsilon\tilde{\beta}\dot{z}^3 + k\left(z^3 - \frac{3}{4}(z_1 + z_2)z^2 + \frac{1}{2}z_1z_2z\right) = \epsilon\tilde{A}\Omega'^2 \sin(\Omega'\tau). \quad (11)$$

Rewriting this second order differential equation as two first order differential equations yields,

$$\begin{aligned} \dot{z} &= v, \\ \dot{v} &= -kz^3 + \frac{3k}{4}(z_1 + z_2)z^2 - \frac{k}{2}z_1z_2z + \epsilon(-\tilde{\alpha}v - \tilde{\beta}v^3 + \tilde{A}\Omega'^2 \sin(\Omega'\tau)). \end{aligned} \quad (12)$$

Note that the unperturbed equations (for $\epsilon = 0$) can be obtained from the gradients of the Hamiltonian $H^0(z, v)$,

$$\dot{z} = \frac{\partial H^0}{\partial v}, \quad \dot{v} = -\frac{\partial H^0}{\partial z}, \quad (13)$$

where H^0 is defined as

$$H^0 = \frac{v^2}{2} + \frac{k}{4}(z - z_1)(z - z_2)z^2. \quad (14)$$

The homoclinic orbits are obtained from the unperturbed Hamiltonian, Eq. (14), as

$$\tau = \sqrt{\frac{2}{-k}} \int \frac{dz}{z\sqrt{(z - z_1)(z - z_2)}}. \quad (15)$$

which may be evaluated in the following form:

$$\tau - \tau_0 = \sqrt{\frac{2}{-z_1 z_2 k}} \ln \left| \frac{2z_1 z_2 - (z_1 + z_2)z + 2\sqrt{z_1 z_2 (z - z_1)(z - z_2)}}{z} \right|, \quad (16)$$

where τ_0 is a time like constant of integration.

Thus, the single homoclinic orbit is given by the inverse of the above expression and the corresponding velocity $(z^*(\tau - \tau_0), v^*(\tau - \tau_0))$, as [28],

$$z^* = \frac{4z_1 z_2 \exp\left((\tau - \tau_0)\sqrt{\frac{-kz_1 z_2}{2}}\right)}{-(z_1 - z_2)^2 - \exp\left(2(\tau - \tau_0)\sqrt{\frac{-kz_1 z_2}{2}}\right) + 2(z_1 + z_2) \exp\left((\tau - \tau_0)\sqrt{\frac{-kz_1 z_2}{2}}\right)} \quad (17)$$

$$v^* = \frac{-4z_1 z_2 \sqrt{\frac{-kz_1 z_2}{2}} \exp\left((\tau - \tau_0)\sqrt{\frac{-kz_1 z_2}{2}}\right) \left((z_1 - z_2)^2 - \exp\left(2(\tau - \tau_0)\sqrt{\frac{-kz_1 z_2}{2}}\right)\right)}{\left(-(z_1 - z_2)^2 - \exp\left(2(\tau - \tau_0)\sqrt{\frac{-kz_1 z_2}{2}}\right) + 2(z_1 + z_2) \exp\left((\tau - \tau_0)\sqrt{\frac{-kz_1 z_2}{2}}\right)\right)^2}.$$

Now suppose that

$$\tau_0 = \tau_{01} + \tau_{02}, \quad \text{where } \tau_{01} = -\ln\left(\frac{\sqrt{2}(z_2 - z_1)}{\sqrt{-kz_1 z_2}}\right). \quad (18)$$

τ_{01} has been fixed to guarantee the proper parity (under the time transformation $\tau \rightarrow -\tau$), and hence

$$z(-\tau) = z(\tau) \quad \text{and} \quad v(-\tau) = -v(\tau). \quad (19)$$

τ_{02} is an arbitrary constant to be determined later in the minimization of the Melnikov integral $M(\tau_{02})$. The corresponding orbit $(z^*(\tau - \tau_0), v^*(\tau - \tau_0))$ is

plotted on the phase plane in Fig. 6.

The distance between perturbed stable and unstable manifolds and their possible cross-sections may be examined by means of the Melnikov integral $M(\tau_{02})$, given by [21]

$$M(\tau_{02}) = \int_{-\infty}^{+\infty} \mathbf{h}(z^*(\tau - \tau_{01} - \tau_{02}), v^*(\tau - \tau_{01} - \tau_{02})) \wedge \mathbf{g}(z^*(\tau - \tau_{01} - \tau_{02}), v^*(\tau - \tau_{01} - \tau_{02})) d\tau, \quad (20)$$

where the wedge product for two dimensional vectors is defined as $\mathbf{h} \wedge \mathbf{g} = h_1 g_2 - h_2 g_1$. The corresponding vector \mathbf{h} is the gradient of unperturbed Hamiltonian (Eq. 13),

$$\mathbf{h} = \left[k(-z^{*3} + \frac{3}{4}(z_1 + z_2)z^{*2} - \frac{1}{2}z_1 z_2 z^*), v^* \right], \quad (21)$$

while the vector \mathbf{g} consists of the perturbation terms to the same Hamiltonian (Eq. (10)),

$$\mathbf{g} = \left[-\tilde{\alpha}v^* - \tilde{\beta}v^{*3} + \tilde{A}\Omega'^2 \sin(\Omega'(\tau)), 0 \right]. \quad (22)$$

Thus, shifting the time coordinate $\tau \rightarrow \tau + \tau_{02}$ under the integral (Eq. (20)), gives

$$M(\tau_{02}) = \int_{-\infty}^{\infty} v^*(\tau - \tau_{01}) \left((-\tilde{\alpha}v^*(\tau - \tau_{01}) - \tilde{\beta}v^{*3}(\tau - \tau_{01}) + \tilde{A}\Omega'^2 \sin(\Omega'(\tau + \tau_{02}))) \right) d\tau. \quad (23)$$

Finally, a sufficient condition for a global homoclinic transition corresponding to a horseshoe type of stable and unstable manifold cross-section (for the excitation amplitude $A > A_c$), can be written as:

$$\bigvee_{\tau_{02}} M(\tau_{02}) = 0 \text{ and } \frac{\partial M(\tau_{02})}{\partial \tau_{02}} \neq 0. \quad (24)$$

From Eqs. (23) and (24)

$$A_c = \frac{I_1}{\Omega'^2 I_2(\Omega')}, \quad (25)$$

where

$$I_1 = \left| \int_{-\infty}^{\infty} (\alpha(v^*(\tau))^2 + \beta(v^*(\tau))^4) d\tau \right| \quad (26)$$

and

$$\begin{aligned} I_2(\Omega') &= \sup_{\tau_{02} \in \mathbb{R}} \left| \int_{-\infty}^{\infty} v^*(\tau - \tau_{01}) \sin(\Omega'(\tau + \tau_{02})) d\tau \right| \\ &= \left| \int_{-\infty}^{\infty} v^*(\tau - \tau_{01}) \sin(\Omega'\tau) d\tau \right|, \end{aligned} \quad (27)$$

where \sup means supremum for various τ_{02} , and is practically realized by

$$\cos(\Omega'\tau_{02}) = \pm 1. \quad (28)$$

Equation 27 has been obtained by using a trigonometric identity: $\sin(\psi_1 + \psi_2) = \sin(\psi_1)\cos(\psi_2) + \cos(\psi_1)\sin(\psi_2)$ where $\psi_1 = \Omega'\tau$ and $\psi_2 = \Omega'\tau_{02}$. We left only the term $\cos(\psi_2)$ (Eq. 28) because of the odd parity of the velocity function $v^*(\tau - \tau_{01})$ under the integral. Of course to do such a simplification we needed defined parity of v^* (Eq. 20) and a proper choice of a constant τ_{01} (Eq. 19).

Note, the above integrals may be evaluated analytically [31] but here, for simplicity, they are calculated numerically [23,28]. Figure 7 shows A_c as a function of Ω' for $\alpha \cong -0.04$ and $\beta \cong 2.69$ (see Eqs. (6) and (7)) given by the curve labelled '1' and $\beta \cong 2.69/2$ given by the curve labelled '2'. One can see the characteristic double sack-like shape, similar to the structure observed by Lenci and Rega [25]. This structure is governed by the oscillating term $\sin(\Omega'\tau)$ in the denominator of the integral $I_2(\Omega')$ (Eq. (25)).

4 Results of Simulations

To illustrate the influence of a global homoclinic transition on the system dynamics, simulations were performed for interesting values of the system parameters, using Eq. (7) for the model in Fig. 1. Knowing the critical value of the road profile amplitude A_c (Fig. 7) and looking at a typical homoclinic bifurcation [22] the effect on the resonance curves were examined first. Figure 8 shows the sequence of resonance curves for $A = 0.11, 0.16, 0.21, 0.26$,

0.31 and 0.36m respectively. Apart from a typical shift of the maximum response to the right all of these curves are very similar, up to $A = 0.31\text{m}$. For $A = 0.41\text{m}$ the synchronized solution is not stable in the region of resonance. The other difference in the system behaviour occurs to the left side of the resonance peak where multiple solutions of the nonlinear system appear (in this case resonant and non-resonant solutions) in the region of the resonance. One can observe that starting from $A = 0.26\text{m}$ the curves in Fig. 8 show a discontinuity signaling jumps between the resonant and non-resonant vibration amplitude A_{OUT} . Note in all cases a series of simulations were performed to calculate the system response, with Ω' decreasing as in Figs. 3a–b. For most of curves the same initial conditions were used for large Ω' , namely $[x_{in}, v_{in}] = [0.15, 0.1]$. However if the system escaped from the potential well initial conditions of $[x_{in}, v_{in}] = [-0.15, 0.1]$ and $[0, 0.1]$ were used to avoid this effect. For $A = 0.36\text{m}$ this was not possible in the vicinity of the resonance peak where the system escaped from the potential well for any initial conditions. Moreover just before this escape (for $A = 0.36\text{m} \approx A_c$) we observe a further increase in the vibration amplitude A_{OUT} . Examining the related bifurcations diagrams we identified period doubling phenomenon occurring in this region which can be classified as a precursor of chaotic vibrations. Indeed alternative criteria to the Melnikov approach (Eq. 24) are based on the period doubling cascade [26,27]. For larger amplitudes the unstable vibration region where escape from the potential is possible increases. On the other hand, at $A = A_c$ the border between the basins of attraction belonging to different solutions disappears. To avoid these difficulties for further analysis the synchronized solution for $\Omega' = 0.8$ at $A = 0.31\text{m}$ (Fig. 8) was used, and then the excitation amplitude was increased slightly to $A = 0.41\text{m}$, crossing the critical amplitude of $A_c \cong 0.35\text{m}$. Figures 9a-b show the phase portraits (by lines) and Poincare maps (by points) for these two cases. Figure 9a shows a synchronized motion while Fig. 9b corresponds to a chaotic attractor. The dominant Lyapunov exponents calculated for these responses are $\lambda_1 = -0.1625$ (Fig. 9a) and $\lambda_1 = 0.03540$ (Fig. 9b). Note, the chaotic attractor is very similar to that studied by Thompson [32] where the harmonic potential has been supplemented by a nonlinear term with displacement to the power 3 (z^3). Figure 9 also shows the time histories for the two cases: $A = 0.31\text{m}$ (Fig. 9c) and $A = 0.41\text{m}$ (Fig. 9d). In this figure the difference between the periodic and chaotic responses is clear.

5 Summary and Conclusions

We have studied the vibrations of a quarter-car model with a softening stiffness of the Duffing type, focusing on the potential for chaotic behaviour. The model and parameters used were taken from the paper by Li *et al.* [6], with

the addition of the gravity force. The addition of this gravity force breaks the symmetry of the potential, so that $V(-x) \neq V(x)$. The hysteretic nature of the damper caused a range of interesting system behaviour, such as quasi-periodic, synchronized and chaotic motion. This had a substantial effect on the heteroclinic orbits, which transformed into homoclinic orbits. We examined the global homoclinic bifurcations that appear as instabilities at the boundaries of the basins of attraction, and the cross-sections of stable and unstable manifolds, by the perturbation approach using Melnikov theory. A critical amplitude was found for which the system can exhibit chaotic vibrations. The analytic results have been confirmed by numerical simulations. In particular, the chaotic strange attractor was found for an excitation amplitude A at the critical value, A_c , and a period doubling precursor for $A = 0.36\text{m}$. The transition to chaos appears to be present for $A_c \cong 0.36\text{m}$ but could be lowered significantly for a smaller damping coefficient c_2 (Fig. 7). Fortunately this region is beyond the usual amplitude of road profile excitation. The chaotic solution appears just before the escape from the potential well, which is similar to the system with a non-symmetric potential described by Thompson [32].

Acknowledgements

This research has been partially supported by the Polish Ministry of Science and Information.

References

- [1] G. Verros, S. Natsiavas, G. Stepan, Control and dynamics of quarter-car models with dual-rate damping, *Journal of Vibration and Control* 6 (2000) 1045–1063.
- [2] M. Gobbi, G. Mastinu, Analytical description and optimization of the dynamic behaviour of passively suspended road vehicles, *J. Sound Vibr.* 245 (2001) 457–481.
- [3] U. von Wagner, On non-linear stochastic dynamics of quarter car models *Int J Non-Linear Mech.* 39 (2004) 753–765.
- [4] S. Turkay, H. Akcay, A study of random vibration characteristics of the quarter-car model *J. Sound Vibr.* 282 (2005) 111–124.
- [5] G. Verros, S. Natsiavas, C. Papadimitriou C Design optimization of quarter-car models with passive and semi-active suspensions under random road excitation, *Journal of Vibration and Control* 11 (2005) 581–606.

- [6] S. Li, S. Yang, W. Guo, Investigation on chaotic motion in histeretic non-linear suspension system with multi-frequency excitations, *Mechanics Research Communications* 31 (2004) 229–236.
- [7] K. Szabelski, W. Samodulski, Drgania układu z niesymetryczną charakterystyką sztywności przy parametrycznych i zewnętrzny wymuszeniu, *Mechanika Teoretyczna i Stosowana* 23 (1985) 223–238.
- [8] K. Szabelski, The vibrations of self-Excited system with parametric excitation and non-symmetric elasticity characteristics, *Journal of Theoretical and Applied Mechanics* 29 (1991) 57–81.
- [9] M. Mitschke, *Dynamik der Kraftfahrzeuge*, Springer, Berlin, 1990.
- [10] D.L. Guo, H.Y. Hu, J.Q. Yi, Neural network control for a semi-active vehicle suspension with a magnetorheological damper *Journal of Vibration and Control* 10 (2004) 461–471.
- [11] H. Liu, K. Nonami, T. Hagiwara, Semi-active fuzzy sliding mode control of full vehicle and suspensions, *Journal of Vibration and Control* 11 (2005) 1025–1042.
- [12] C. Lauwerys, J. Swevers, P. Sas, Robust linear control of an active suspension on a quarter car test-rig, *Control Engineering Practice* 13 (2005) 577–586.
- [13] S.-B. Choi and S.-K. Lee, A hysteresis model for the field-dependent damping force of a magnetorheological damper, *J. Sound Vibr.* 245 (2001) 375–383.
- [14] C.Y. Lai, W.H. Liao, Vibration control of a suspension system via a magnetorhellogical fluid damper, *Journal of Vibration and Control* 8 (2002) 527–547.
- [15] H. Du, K.Y. Sze, J. Lam, Semi-active H (∞) control of vehicle suspension with magneto-rheological dampers, *J. Sound Vibr.* 283 (2005) 981–996.
- [16] D.C. Karnopp, M.J. Crosby and R.A. Harwood, Vibration control using semi-active force generators, *Transactions of the ASME, Journal of Engineering for Industry*, (1974) 619–626.
- [17] P. Soravia, H_∞ control of nonlinear systems: Differential games and viscosity solutions, *SIAM J. Control and Optimization*, 34 (1996) 1071–1097.
- [18] Q. Zhu, M. Ishitobi, Chaos and bifurcations in a nonlinear vehicle model, *J. Sound Vibr.* 275 (2004) 1136–1146.
- [19] Q. Zhu, M. Ishitobi, Chaotic vibration of a nonlinear full-vehicle model, *International Journal of Solids and Structures* 43 (2006) 747–759.
- [20] V. K. Melnikov, On the stability of the center for time periodic perturbations, *Trans. Moscow Math. Soc.* 12 (1963) 1–57.
- [21] J. Guckenheimer, P. Holmes, *Nonlinear Oscillations, Dynamical Systems and Bifurcations of Vectorfields*, Springer, New York 1983.

- [22] E. Tyrkiel, On the role of chaotic saddles in generating chaotic dynamics in nonlinear driven oscillators, *Int. J. Bifurcation and Chaos* 15 (2005) 1215–1238.
- [23] G. Ciocogna, F. Popoff, Asymmetric Duffing equation and the appearance of chaos, *Europhysics Letters* 3 (1987) 963–967.
- [24] V. Brunsden, J. Coetell, P.J. Holmes, Power spectra of chaotic vibrations of a buckled beam, *J. Sound Vibr.* 130 (1989) 561–577.
- [25] S. Lenci and G. Rega, A unified control framework of the non-regular dynamics of mechanical oscillators, *J. Sound and Vibr.* 278 (2004) 1051–1080.
- [26] W. Szemplińska-Stupnicka, The refined approximate criterion for chaos in a two-state mechanical systems, *Ingenieur Archiv.* 58 (1988) 554–566.
- [27] T. Kapitaniak, *Chaotic Oscillations in Mechanical Systems*, Manchester University Press, Manchester 1991.
- [28] G. Litak, M. Borowiec, Oscillators with asymmetric single and double well potentials: transition to chaos revisited, *Acta Mechanika* (2005) submitted.
- [29] G. Litak, G. Spuz-Szpos, K. Szabelski, J. Warmiński, Vibration analysis of self-excited system with parametric forcing and nonlinear stiffness, *Int. J. Bifurcation and Chaos* 9 (1999) 493–504.
- [30] J.L. Trueba, J. Rams, M.A.F. Sanjuan, Analytical estimates of the effect of nonlinear damping in some nonlinear oscillators *Int. J. Bifurcation and Chaos* 10 (2000) 2257–2267.
- [31] B. Bruhn, B-P. Koch, G. Schmidt, On the onset of chaotic dynamics in asymmetric oscillators, *Z. Angew. Math Mech.* 74 (1994) 325–331.
- [32] JMT Thompson, Chaotic phenomena triggering the escape from a potential well., *Proceedings of the Royal Society of London A* 421 (1989) 195–225.

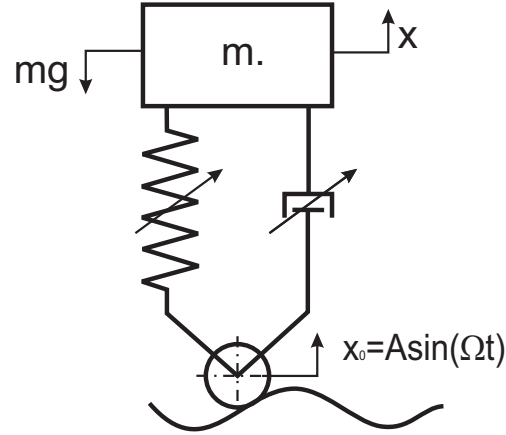


Fig. 1. The quarter-car model subjected to kinematic excitation with nonlinear damping and stiffness.

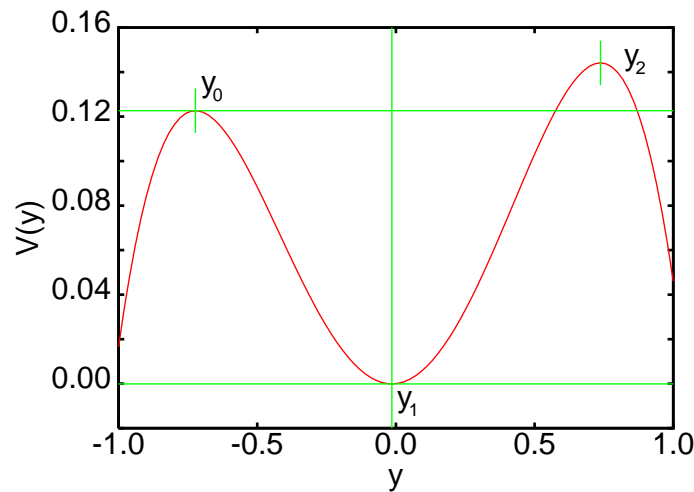


Fig. 2. External potential $V(y)$ (Eq. (8)) for given system parameters (Eq. (6)). $V(y)$ is scaled in Nm while y is in m. The fixed points are $y_0 = -0.7228\text{m}$, $y_1 = -0.0147\text{m}$, $y_2 = 0.7375\text{m}$.

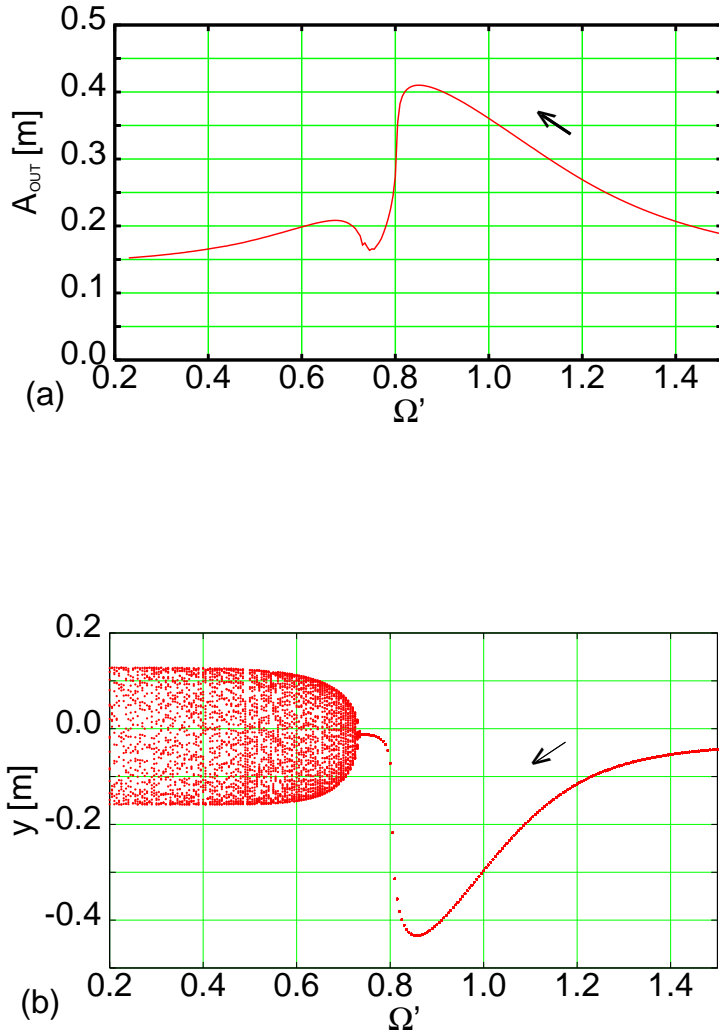


Fig. 3. Vibration amplitude $A_{OUT} = (y_{max} - y_{min})/2$ (Fig. 3a) and bifurcation diagram (Fig. 3b). The amplitude of a road profile has been taken as $A = 0.11\text{m}$. The arrows indicates Ω' reduces in the simulations. For each new smaller Ω' the initial conditions $[y_{in}, v_{in}]$ were taken as the final position and velocity for the previous Ω' .

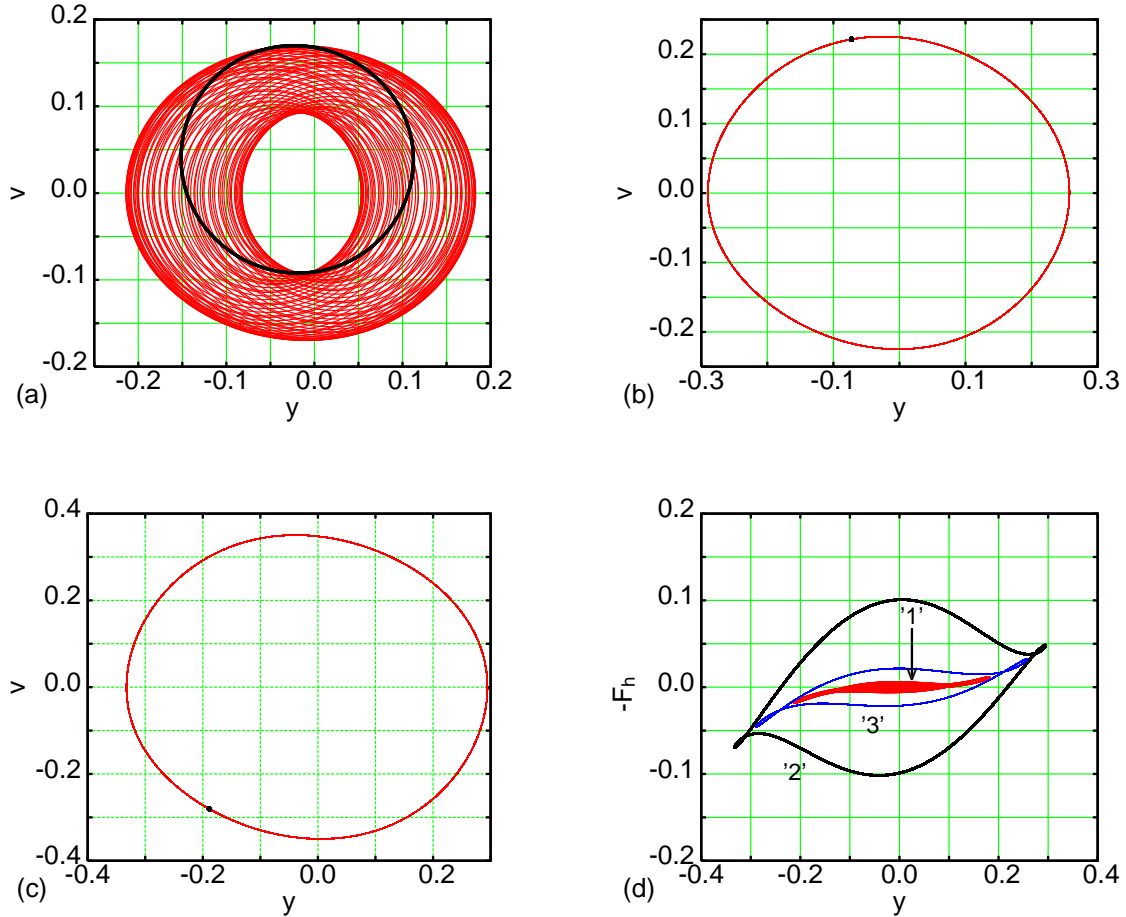


Fig. 4. Phase diagrams (velocity $v = \dot{y}$ versus displacement y plotted by lines) and corresponding Poincare sections (plotted by points) for $A = 0.11\text{m}$ and different Ω' : $\Omega' = 0.6$ (Fig. 4a), $\Omega' = 0.8$ (Fig. 4b) and $\Omega' = 1.1$ (4c). The corresponding hysteresis curves are shown in Fig. 4d, where '1', '2' and '3' represent $\Omega' = 0.6$, 0.8 and 1.1, respectively. $v\omega$ is scaled in m/s, y in m, while the renormalized F_h is presented in dimensionless units $F_h = \alpha\dot{y} + \beta\dot{y}^3 + ky^3$ (see Eq. (7)).

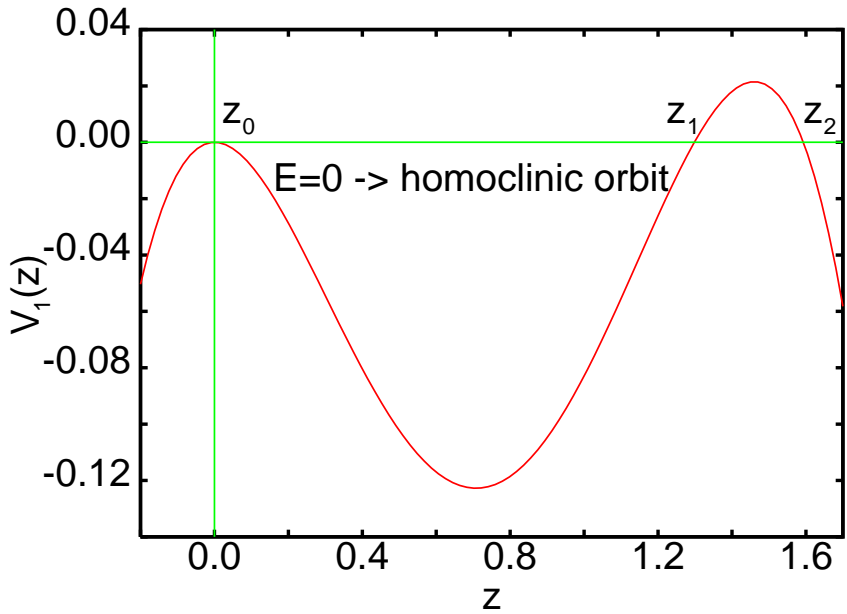


Fig. 5. Renormalized external potential $V_1(z) = \frac{k}{4}z^2(z-z_1)(z-z_2)$ for given system parameters (in our case: $k = -1.875 \text{ N/m}^3$, $z_1 \approx 1.298\text{m}$ and $z_2 \approx 1.593\text{m}$). z is expressed in m while $V(z)$ is in Nm.

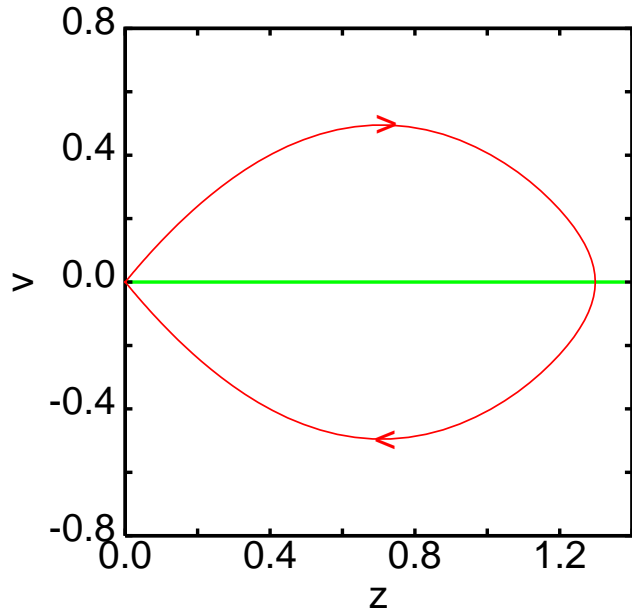


Fig. 6. A homoclinic orbit for the given potential (Eq. (9) and Fig. 5). z is expressed in m while $v\omega$ is given in m/s.

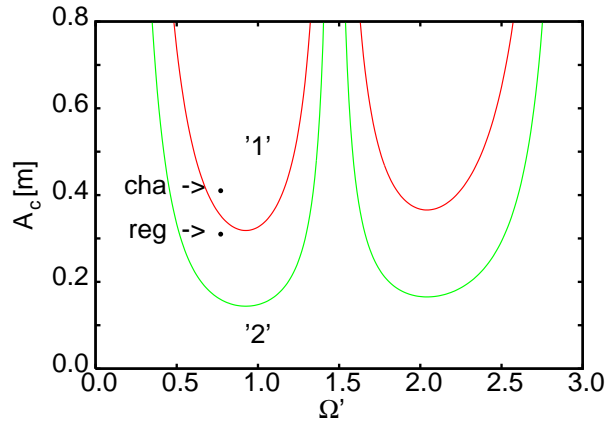


Fig. 7. Critical amplitude A_c versus vibration frequency for two different damping choice. The damping coefficients $c_2 = 25 \text{ Ns}^3/\text{m}^3$ (for other system parameters see Eq. (6)) , and $c_2 = 12.5 \text{ Ns}^3/\text{m}^3$, for '1' and '2' curves respectively. The points 'reg' and 'cha' denote regular and chaotic solutions (to be examined later in Figs. 9a and b).

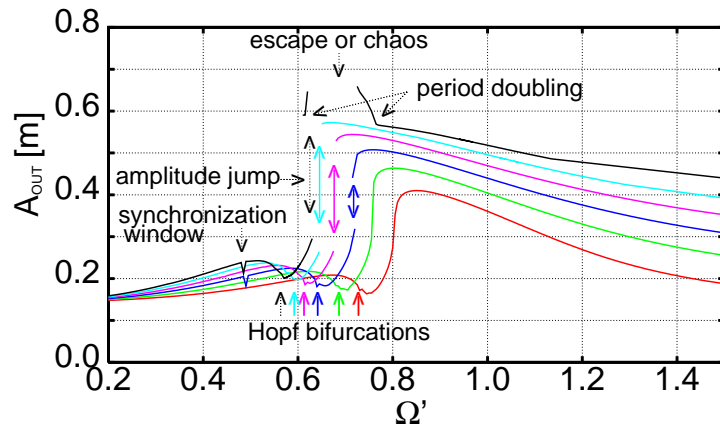


Fig. 8. Sequence of vehicle vibration amplitudes $A_{OUT} = (y_{max} - y_{min})/2$ versus frequency Ω' for road profile amplitudes of $A = 0.11, 0.16, 0.21, 0.26, 0.31$ and 0.36m (from the lower to upper curves, respectively).

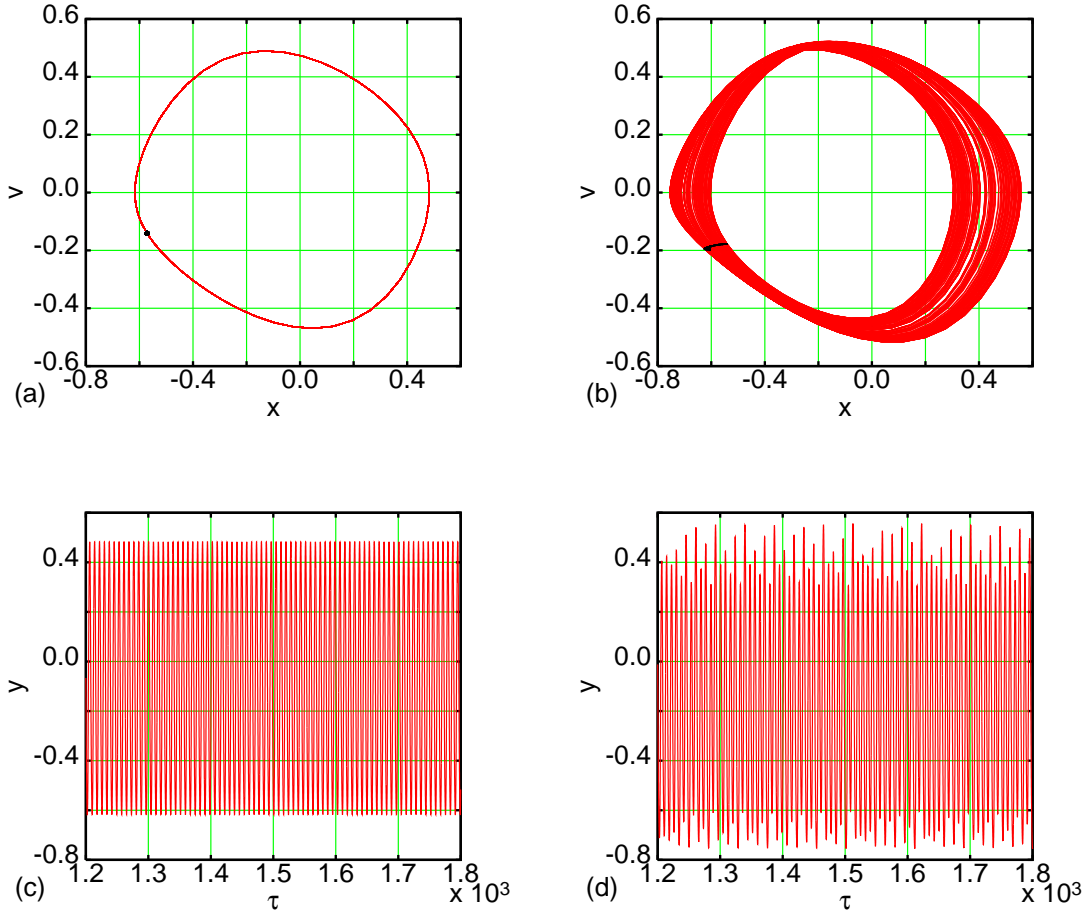


Fig. 9. Phase portraits and Poincare maps below and above the critical amplitude at $\Omega' = 0.8$ for regular (Fig. 9a, $A = 0.31\text{m}$ and initial conditions $[x_{in}, v_{in}] = [0.15, 0.1]$) and chaotic (Fig. 9b, $A = 0.41\text{m}$ and the initial conditions $[x_{in}, v_{in}] = [-0.15, 0.1]$) solutions. The dominant Lyapunov exponents are $\lambda_1 = -0.1625$ and $\lambda_1 = 0.0354$, respectively. Figs. 9c and 9d give the corresponding time responses. Here $v\omega$ is given in m/s while y is in m .